Advanced Functional Materials

ADVANCED FUNCTIONAL MATERIALS
www.afm-journal.de

RESEARCH ARTICLE OPEN ACCESS

Conformal Polymer Electrolyte Enabled by Nitrile Coordination for Long-Cycle Solid-State Lithium Metal Batteries

Liyuan Huang[1] | Liang Lan[1] | Yifan Wu[1] | Xin Ao[1] | Naigen Zhou[1] | Yi Zhou[1] | Chengjin Peng[1] | Yecheng Liu[1] | Shan Fang[1] | Stefano Passerini[2,3,4]

[1]School of Physics and Materials Science, Nanchang University, Nanchang, Jiangxi, China | [2]Helmholtz Institute Ulm (HIU), Ulm, Germany | [3]Karlsruhe Institute of Technology (KIT), Karlsruhe, Germany | [4]Austrian Institute of Technology (AIT), Center For Transport Technologies, Wien, Austria

Correspondence: Shan Fang (fangshan@ncu.edu.cn) | Stefano Passerini (stefano.passerini@kit.edu)

Received: 5 November 2025 | **Revised:** 7 December 2025 | **Accepted:** 15 December 2025

Keywords: in situ situ solidification | lithium metal batteries | polymer solid-state electrolytes | solid electrolyte interphase

Abstract

Lithium metal is a highly promising anode for next-generation high-energy-density batteries due to its high theoretical capacity, yet its practical application remains hindered by poor interfacial compatibility with polymer solid-state electrolytes (PSEs). Herein, an in situ solidification PSE that utilizes poly(ethyleneglycol)methyletheracrylate (PEGMEA) and methylated pivalonitrile (PN) is developed (PNF), which forms an conformal and mechanically robust solid electrolyte interphase (SEI) on the lithium metal surface. The coordination between the nitrile group (–C≡N) and Li^+ regulates interfacial ion transport, while the formed organic–inorganic (hybrid) SEI effectively combines mechanical flexibility and interfacial rigidity to buffer lithium volume fluctuations and inhibit dendrite growth. Benefiting from the enhanced Li^+ hopping sites and improved ionic mobility, the PNF electrolyte exhibits high ionic conductivity, i.e., 3.47×10^{-4} S cm^{-1} at 30°C. Li|PNF|Li symmetric cells show exceptional cycling stability, surpassing 1000 h at 0.5 mA cm^{-2}. Notably, Li|PNF|$LiFePO_4$ cells achieve a capacity retention of 92.8% after 1000 cycles at 0.5C and 78.9% after 2000 cycles at 1C rate, both at 30°C, highlighting the exceptional conformal properties of the electrolyte resulting in the superior cycling performance. This study establishes a design framework for constructing long-term cycling, solid-state lithium-metal batteries through tailored interfacial engineering of PSEs.

1 | Introduction

To overcome the energy density limitations of traditional lithium-ion batteries (LIBs) and meet the escalating global demand for energy storage, the development of novel secondary batteries with high performance and enhanced safety is imperative [1, 2]. Compared to LIBs employing graphite anodes, lithium metal batteries (LMBs), which utilize lithium metal as the anode, have attracted significant research interest due to the anode remarkably high theoretical specific capacity (3860 mAh·g^{-1}) and low redox potential (−3.04 V vs. SHE) [3, 4]. Among these, solid-state lithium metal batteries (SLMBs) have emerged as a primary research focus owing to their high energy density and superior safety profile [5–7]. However, the advancement of current LMBs based on inorganic solid electrolytes (ISEs) is significantly hindered by their high solid–solid interfacial contact resistance and the inherent challenges associated with the rigid nature of ISEs during battery assembly and large-scale manufacturing [8–10]. Polymer solid electrolytes (PSEs), as one of the promising electrolyte candidates for LMBs, are considered more attractive solid electrolyte materials due to their tunable mechanical stability, excellent processability, and

favorable interfacial compatibility [11–13]. Among the various PSE fabrication techniques, the in situ curing method stands out for its exceptional operational convenience. This method demonstrates high compatibility with existing battery manufacturing processes and effectively addresses interfacial contact issues between SEs and electrodes [14, 15]. Consequently, PSEs fabricated via in situ curing technology exhibit substantial application potential for high-capacity LMBs [16].

PEGMEA, a commonly used polymeric monomer for PSEs, exhibits excellent compatibility with lithium metal. However, the low ionic conductivity of PEGMEA-based PSEs (10^{-6}–10^{-5} S cm^{-1} at 25°C) constrains their application in LMBs [5, 17]. To improve the ionic conductivity of PEGMEA-based PSEs, Cui et al. fabricated a homogeneous sulfide/polymer composite solid electrolyte through in situ polymerization of PEGMEA monomers on a freestanding porous sulfide skeleton [18]. This design establishes continuous Li^+ conduction pathways through both the sulfide phase and the resulting sulfide/polymer interface, simultaneously delivering high ionic conductivity and compatible electrolyte/electrode interfaces. Nevertheless, this scaffold-based polymerization method involves complex procedures incompatible with industrial-scale production. Subsequently, Liu et al. synthesized a eutectic PSE through in situ polymerization of succinonitrile (SN) with PEGMEA [19]. The interaction between PEGMEA and SN facilitates the dissociation of LiDFOB, leading to elevated ionic conductivity (1.30 mS cm^{-1}). The —C≡N group in SN serves as a strong electron-withdrawing moiety that effectively enhances lithium salt dissociation, while also exhibiting excellent oxidation resistance and thermal stability. Consequently, many nitrile-based additives, primarily based on SN, have been extensively studied [15, 20–22]. However, the presence of —C≡N inevitably introduces α-hydrogen on adjacent carbon atoms [23], which increases reactivity toward lithium metal. This imposes limitations on the application of nitrile-based additives in PSEs [21].

Inspired by the finding that methyl substitution at the α-hydrogen successfully addresses lithium metal incompatibility concerns [24], pivalonitrile (PN)—a relatively underexplored nitrile compound—was employed as a plasticizing additive for polymer chains. Compared to acetonitrile (AN), PN exhibits superior stability due to complete methyl substitution at α-hydrogen atoms. This molecular design significantly suppresses reactivity with lithium metal, resulting in exceptional interfacial compatibility in PN-incorporated PSE. Additionally, the strong electron-withdrawing —C≡N group in PN enables robust coordination with Li^+ ions, facilitating more Li^+ dissociation from LiTFSI and consequently enhancing ionic conductivity [25]. As a result, the PNF electrolyte, synthesized from PEGMEA monomer, LiTFSI, PN, and FEC, achieves an ionic conductivity of 3.47×10^{-4} S cm^{-1} at 30°C. Lithium symmetric cells constructed with PNF electrolyte exhibit exceptional cycling stability, operating for over 1000 h at current densities of 0.3 and 0.5 mA cm^{-2}. Additionally, Li|PNF|$LiFePO_4$ cells demonstrate outstanding long-term cycling performance, with a capacity retention of 78.9% after 2000 cycles at 1C (30°C) and 92.6% after 1000 cycles at 0.5C (30°C). Notably, the pouch cell constructed with the PNF electrolyte demonstrates safe operation under harsh testing circumstances, highlighting its strong potential for practical SLMBs applications.

2 | Result and Discussion

2.1 | Preparation and Physicochemical Properties of PNF Electrolyte

PEGMEA was chosen as the polymer matrix because of its exceptional mechanical properties and favorable interfacial compatibility with lithium metal [26, 27], and PN served as a plasticizer to improve ionic conductivity. As a methylated derivative of acetonitrile (AN), PN exhibits enhanced electrochemical stability [28], as confirmed by density functional theory (DFT) calculations (Figure 1a). Analysis of the LUMO energies of PN and AN, reveals that PN possesses a higher LUMO energy level (0.558 eV) than AN (0.428 eV), indicating greater resistance to reductive decomposition. Stored lithium metal in PN and AN, respectively, Figure S1 shows that lithium metal demonstrates superior stability in PN compared to AN. Simultaneously, PN exhibits a more uniform electron density distribution, indicating significantly reduced molecular polarization due to methyl substitution. These features collectively improve the cycling stability of LMBs. A precursor solution was prepared using PEGMEA monomer as the polymeric matrix, incorporating PN, FEC, and LiTFSI. The role of FEC is to preferentially decompose, yielding a uniform LiF-containing SEI layer on the lithium metal surface, preventing subsequent side reactions of other electrolyte components. The solution was thermally cured at 65°C for 12 h, during which AIBN initiated the free-radical polymerization of PEGMEA to synthesize the solid-state PNF electrolyte (Figure 1b). Optical images of the cured electrolytes with different PN proportions are shown in Figure S2. When the PN content reaches 40 vol%, the solution cannot be fully cured upon heating. The ionic conductivity of the electrolyte was tested via electrochemical impedance spectroscopy (EIS). As shown in Figure S3, the data reveal that the conductivity rises according to the PN content increase. This can be attributed to the additional lithium-ion migration sites provided by the incorporation of PN, which increases the free volume for polymer segmental motion. Furthermore, Li||Li symmetric cells were assembled using electrolytes containing 10 vol%, 20 vol%, and 30 vol% PN, and subjected to cycling tests (see Figure S4). Based on a comprehensive evaluation of the post-curing morphology, the polarization voltage from cycling tests, and the conductivity test, the composition with 30 vol% PN, later on named PNF electrolyte, was determined to be optimal. Figure 1c presents optical photographs of the PNF electrolyte precursor solution before and after polymerization, confirming the successful polymerization of PEGMEA monomers following thermal treatment. Furthermore, the consistency of the electrolyte has been examined. As shown in Figure 1c, the electrolyte can withstand stretching deformations without fracturing, i.e., the PNF electrolyte is still capable of preserving the mechanical properties of P(PEGMEA) while incorporating PN. Figures 1d,e show SEM images of PNF before and after it was filled into the GF/A glass fiber separator (GFA). The microporous structure of the GFA enables thorough penetration of the precursor solution, which, upon thermal curing, forms continuous Li^+ conduction pathways. Cross-sectional SEM images reveal close contact among the $LiFePO_4$ cathode, the in situ-formed PNF electrolyte, and Li metal anode (Figure S5), highlighting the structural integrity of the assembled cell. The structure of the PNF was characterized using Fourier-transform

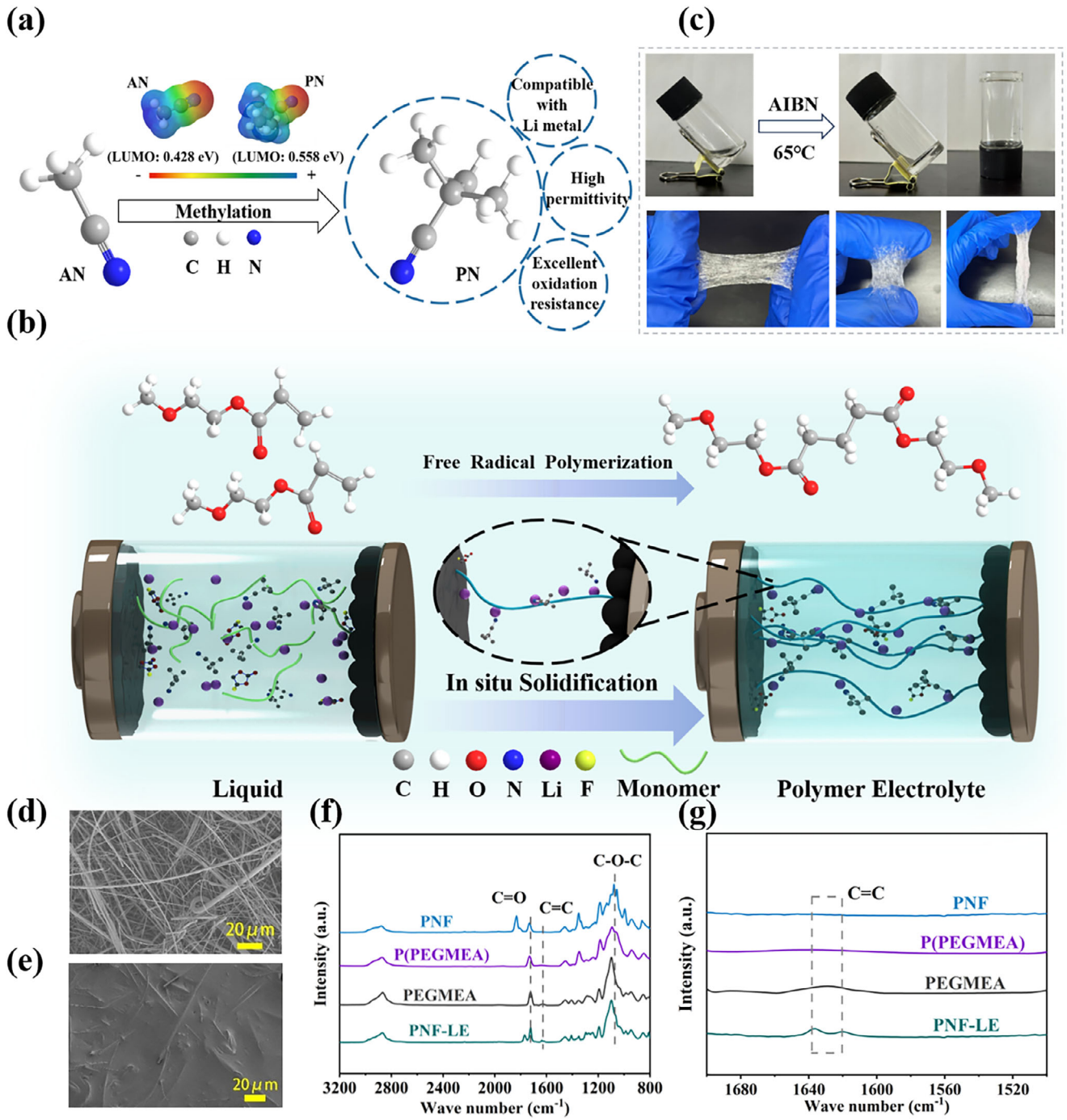

FIGURE 1 | (a) Methylation of AN to form PN and iso-surface of charge distribution for both molecules. (b) Schematic diagram of the in situ preparation of a polymer electrolyte. (c) Optical photographs of the electrolyte before and after curing (top) as well as upon stretching after curing (bottom). SEM image of (d) the GFA and (e) the PNF electrolyte. (f) Full and (g) locally magnified FT-IR spectra of PNF, P(PEGMEA), PEGMEA, and PNF-LE.

infrared spectroscopy (FT-IR). Among them, PNF-LE is the precursor solution, which refers to the solution before curing. Figure 1f displays peaks corresponding to C—O—C (1010 to 1068 cm^{-1}), C═C (1610 to 1650 cm^{-1}), and C═O (1695 to 1750 cm^{-1}). The enlarged view of the infrared spectrum in Figure 1g reveals that after thermal treatment, the C═C bond functional group in PEGMEA at 1630 cm^{-1} disappears, while other functional groups, such as C═O and C—O—C, remain unchanged, indicating the successful polymerization of PEGMEA into P(PEGMEA) [18]. To further evaluate the stability of PN against lithium metal, FTIR spectra were collected for both cycled and pristine PNF electrolytes (Figure S6). The characteristic peaks corresponding to —CN, C—O—C, and C═O groups remained virtually unchanged after cycling, demonstrating good compatibility between the PNF electrolyte and lithium metal. Furthermore, the PNF exhibits excellent thermal stability (Figure S7), guaranteeing its secure utilization post-assembly in batteries. Additionally, linear sweep voltammetry (LSV) (Figure S8) reveals a wide electrochemical

window of up to 5.1 V, suggesting its potential compatibility with high-voltage cathodes.

2.2 | Li^+ migration Mechanism of PNF Electrolyte

As shown in Figure S3, the ionic conductivity of the PNF electrolyte (3.47×10^{-4} S cm^{-1}) is significantly higher than that of the P(PEGMEA) polymer (5.3×10^{-5} S cm^{-1}). The calculated Li^+ transference number (t_{Li^+}) also improves from 0.14 for P(PEGMEA) to 0.23 for PNF (Figure S9a,b). The substantial improvement in both conductivity and t_{Li^+} is attributed to the incorporation of PN, which serves dual functions: (i) acting as a plasticizer to increase the free volume and enhance PEGMEA segmental mobility, and (ii) providing additional Li^+ migration sites through coordination with the nitrile (–C≡N) moieties [29]. To elucidate the underlying conduction mechanism, FTIR spectroscopy was conducted. Observations revealed two distinct peaks at 2233 and 2240 cm^{-1} (Figure 2a), corresponding to the —C≡N group and its coordination with Li^+, respectively, confirming that PN coordinates effectively with Li^+ in the PNF. This results in an increased dissociation of Li^+ from LiTFSI, facilitating the formation of free Li^+, and creation of new, continuous pathways for Li^+ transport between polymer segments, both effects explaining why PNF exhibits higher ionic conductivity and Li^+ transference numbers than P(PEGMEA). Additionally, a significant coordination peak corresponding to Li^+—C—O—C was observed around 1294 cm^{-1} (Figure 2b), indicating a strong interaction between Li^+ and the ether groups in the PEGMEA segments, also contributing to the formation of continuous channels for Li^+ transport [30]. Furthermore, Raman spectroscopy results (Figure 2c) indicate that the free $TFSI^-$ peak in PNF experiences a redshift compared to P(PEGMEA), suggesting that the degree of dissociation of LiTFSI in PNF is significantly higher than that in P(PEGMEA) [31]. In Figure S10, the normalization and peak deconvolution of Raman spectra revealed that in the PNF system, the proportion of $TFSI^-$ in the ion aggregate state was significantly decreased, while the fraction of free $TFSI^-$ anions markedly increased. These findings further confirm that the incorporation of PN promotes the dissociation between Li^+ and $TFSI^-$, thus, modifying the solvation structure of Li^+. Therefore, it can be inferred that there are primarily two pathways for Li^+ migration in PNF (Figure 2d): (i) Li^+ migrates by coordinating with the C═O and C—O—C functional groups in the PEGMEA segments, facilitating transitions between the PEGMEA chains; (ii) The presence of the electron-withdrawing –C≡N groups in PN introduces new interchain hopping sites, enabling Li^+ to transition from PEGMEA's polar groups to PN and then bridge to another PEGMEA segment. These synergistic pathways collectively facilitate efficient and rapid Li^+ transport within the polymer matrix.

Molecular dynamics (MD) simulations were utilized to explore the impact of intermolecular interactions on Li^+ transport in P(PEGMEA) and PNF, aiming to provide a molecular-level understanding of their ion transport mechanisms. Figures 2e,g illustrate the radial distribution functions (RDF) and coordination numbers (CN) for P(PEGMEA) and PNF, while the corresponding molecular snapshots are shown in Figure 2 f,h. Figure 2e illustrates that in P(PEGMEA), the RDF of the O atom from $TFSI^-$ interacting with Li^+ shows a sharp peak at 2.1 Å, corresponding to a CN of 0.22, and the RDF of the O atom from PEGMEA with Li^+ exhibits a sharp coordination peak at 2.03 Å, corresponding to a CN of 4.5. In contrast, the PNF system (Figure 2g) exhibits reduced CN of 3.4 for Li^+–O(PEGMEA) and 0.17 for Li^+-O($TFSI^-$), suggesting a weakening of these coordination interactions. Notably, Figure 2i indicates that the RDF of the N atom in PN with Li^+ shows a sharp peak at 2.2 Å. This suggests that the presence of PN competes for coordination with the C═O and C—O—C groups in PEGMEA, due to the strong electron-withdrawing effect of —C≡N, thereby reducing the coordination number of Li^+ with the O atoms in PEGMEA. This disruption in the conventional coordination environment promotes more dynamic Li^+ hopping between solvation sites, facilitating faster ion transport. The decrease in the coordination number of Li^+ with the O atoms of $TFSI^-$ further confirms that PN promotes the dissociation of Li^+ from LiTFSI, resulting in the improvement of both the ionic conductivity and the Li^+ transference number [28, 32, 33]. Additionally, the primary transport pathway of lithium ions within the PNF system was investigated by calculating the binding energies of PEGMEA and PN with Li^+ ions. As shown in Figure 2j, the binding energy between PN and Li^+ is significantly lower than that of C═O and C–O–C groups. A higher binding energy can hinder dissociation of Li^+ ions, thereby hindering their rapid migration [34]. In contrast, the lower binding energy of PN enables it to act as an intermediate hopping site for Li^+ transport, facilitating ion migration between polymer segments. Therefore, in P(PEGMEA), Li^+ migration primarily relies on the free movement of PEGMEA chains, whereas in the PNF system, PN introduces new hopping sites, weakening Li^+-PEGMEA coordination and enhancing ion migration. In fact, the calculated activation energy (E_a) for Li^+ migration in PNF is 0.302 eV, significantly lower than the 0.390 eV for P(PEGMEA) (Figure S11). Therefore, the high ionic conductivity, low activation energy, and continuous Li^+ transport channels in PNF are expected to enhance battery performance, particularly during cycling at higher current densities [35].

2.3 | Electrochemical Performances of Li|Li Symmetric Cells and Interphase Characterization

To evaluate the electrochemical stability of PNF in relation to lithium metal and compare it with other electrolytes, three types of symmetric cells, i.e., Li|PNF|Li, Li|PAF|Li (in PAF, PN is replaced by AN), and Li|P(PEGMEA)|Li, were constructed. Figure 3a shows the voltage profiles of the Li|PNF|Li cell upon galvanostatic lithium plating/stripping at a fixed areal capacity of 0.1 mAh cm^{-2}, with the current density stepwise increased from 0.1 to 1 mA cm^{-2}. As expected, the polarization voltage escalates with increasing current densities, however, even at 1 mA cm^{-2}, the symmetric cells demonstrate stable polarization without experiencing short-circuit failure. When the current density is reduced back to 0.5 mA cm^{-2}, stable operation is maintained. In stark contrast, the Li|PAF|Li symmetric cell exhibits pronounced voltage instability when the current density exceeds 0.4 mA cm^{-2} (Figure S12a). Upon reverting to 0.5 mA cm^{-2}, the cell experiences complete short-circuit failure after 380 h. Furthermore, when operated at 0.3 mA cm^{-2} (Figure S12b), the Li|PAF|Li symmetric cell swiftly demonstrated escalating polarization and experienced short-circuit failure after 360 h. This failure mechanism is likely due to severe parasitic reactions involving reactive α-hydrogens in

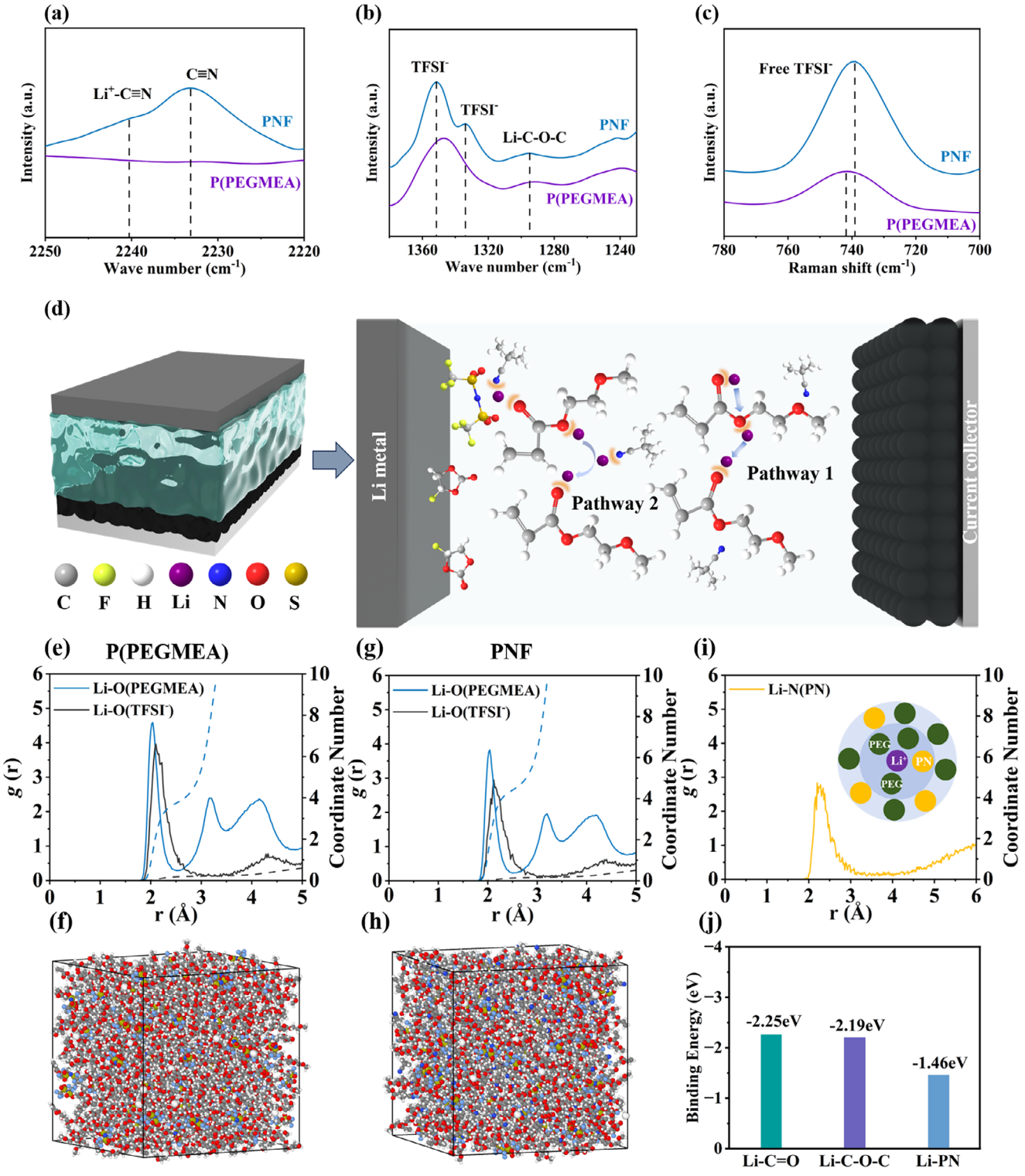

FIGURE 2 | FTIR spectra of PNF and P(PEGMEA) in the range of (a) 2220–2250 cm^{-1} and (b) 1230–1380 cm^{-1}. (c) Raman spectra of PNF and P(PEGMEA). (d) Schematic diagram of Li^+ migration pathways in PNF electrolyte. Radial distribution function (RDF) and molecular snapshot of (e, f) P(PEGMEA) and (g, h) PNF. (i) RDF of PN and Li^+ in PNF. (j) Binding energy of Li-C═O, Li—C—O—C, and Li-PN.

AN and lithium metal. In contrast, the Li|PNF|Li symmetric cell demonstrates stable operation for over 1000 h at current densities of 0.3 and 0.5 mA cm^{-2} (Figure 3b,c). The magnified voltage profile sections at different cycling intervals (Figure S13a,b) show stability without significant fluctuations or short circuits, thus confirming exceptional interfacial and, more in general, electrochemical stability in contact with Li metal electrodes. Therefore, both computational simulations and electrochemical validation indicate that the methylated nitrile-plasticized PNF electrolyte exhibits significantly enhanced stability with lithium metal and excellent Li^+ immigration. Additionally, galvanostatic plating/stripping tests conducted on Li|PNF|Li symmetric cells

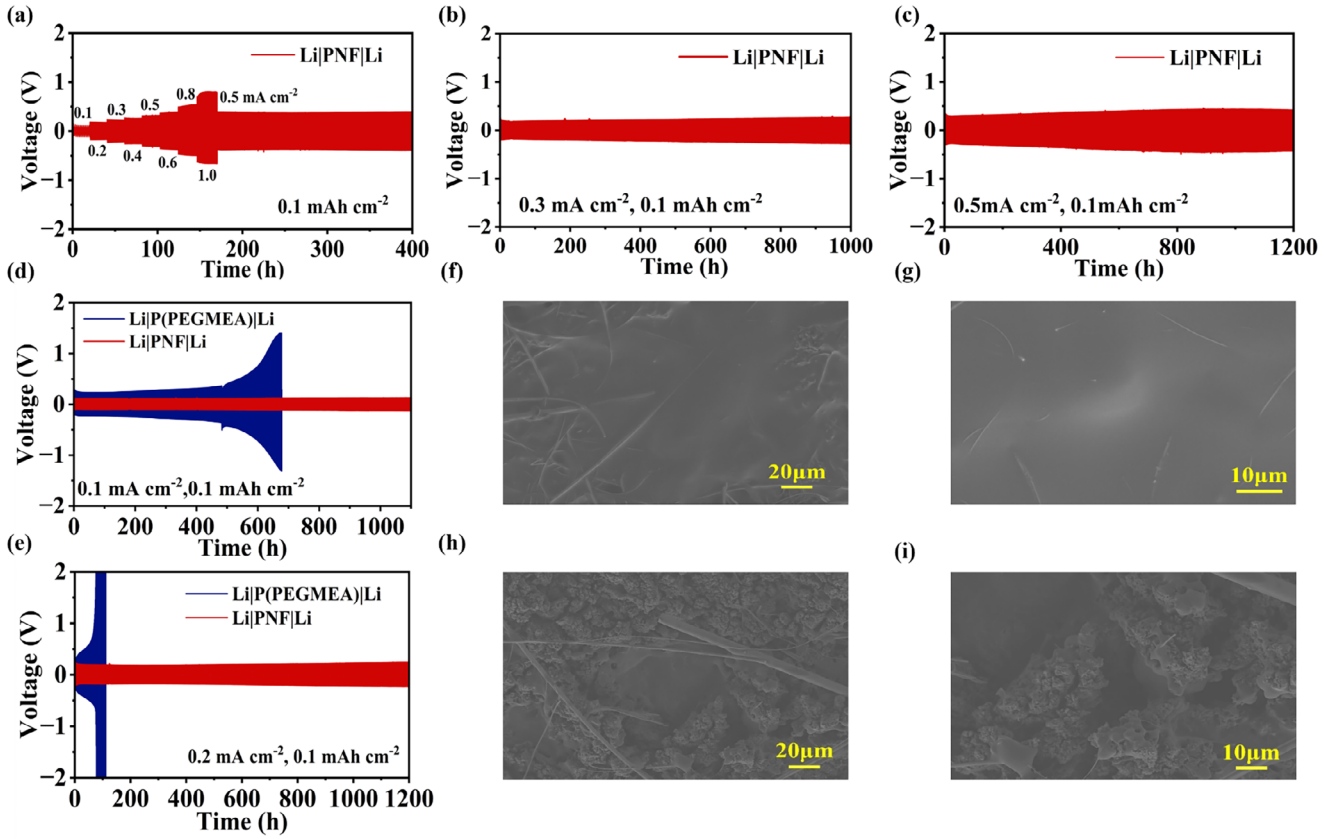

FIGURE 3 | Galvanostatic plating/stripping curves of Li|Li symmetric cells at 30°C. Li|PNF|Li cells upon (a) various current densities, (b) 0.3 mA cm^{-2}, (c) 0.5 mA cm^{-2}. Comparison of Li|PNF|Li and Li|P(PEGMEA)|Li symmetric cells upon cycling at (d) 0.1 mA cm^{-2} and (e) 0.2 mA cm^{-2}, fixed deposition capacity of 0.1 mAh cm^{-2}. SEM images of cycled Li metal electrodes collected from (f and g) Li|PNF|Li and (h and i) Li|P(PEGMEA)|Li symmetric cells.

(Figure 3d,e) reveal that PNF cycles stably for over 1000 h at both 0.1 and 0.2 mA cm^{-2}, while P(PEGMEA) experiences short-circuit failures after 650 and 50 h, respectively. EIS performed after 100 cycles (Figure S14) shows a significantly lower interfacial impedance for PNF (~330 Ω) compared to P(PEGMEA) (~792 Ω), which can be attributed to the formation of a homogeneous, robust, thus thin, SEI layer at the PNF/Li interface during cycling, facilitating rapid Li^+ transport and ensuring stable cell operation [36]. The formation of a uniform, thin SEI can be further attributed to the preferential reduction of FEC (lowest LUMO) in PNF, which favors the formation of an uniform LiF layer in turn suppressing subsequent reactions of other electrolyte components (e.g., PEGMEA) at the Li surface. To elucidate the intrinsic mechanism behind the remarkable electrochemical stability of PNF in contact with Li, the surface morphology of the Li electrodes was characterized using SEM (Figure 3f,g). The lithium surface formed with PNF displays a smooth morphology, devoid of dendritic growth or irregular lithium deposition, and features a thin, uniform composite interphase layer (Figure S15). In contrast, the Li electrode cycled in contact with P(PEGMEA) shows significant nonuniform deposition (Figure 3h,i).

To elucidate the chemical composition and properties of the SEI layer, X-ray photoelectron spectroscopy (XPS) (Figure 4a,b) and energy level diagrams (Figure 4c) were performed to analyze the surface of cycled Li metal electrodes. The XPS spectra taken on Li electrodes extracted from P(PEGMEA)- and PNF-based cells (Figure 4a,b) reveal distinct peaks for C–O, C═O, and C–C bonds, indicating the SEI comprises a substantial proportion of organic species, likely originating from the in situ polymerization on the lithium metal surface [37]. Nevertheless, the PNF system shows a higher content of inorganic elements compared to P(PEGMEA). The F1s spectra reveal LiF peak (684.7 eV) and -CF_3 peak (688.4 eV). In the PNF electrolyte, FEC was reduced preferentially on the lithium metal anode surface due to its lowest LUMO energy level, forming a LiF-rich interphase. This interphase effectively blocks direct contact between $TFSI^-$ anions and lithium metal, thereby suppressing their decomposition. Simultaneously, the introduction of PN promotes the dissociation of the lithium salt, increasing the concentration of free $TFSI^-$ in the system. Consequently, a significant -CF_3 signal along with a certain amount of LiF is detected on the lithium surface in the PNF system. In contrast, in the P(PEGMEA) system without FEC, the lack of a preformed protective layer allows massive reduction of $TFSI^-$ on the lithium metal, resulting in a LiF signal more intense than the -CF_3 signal. Furthermore, comparative analysis of N1s spectra reveals higher Li_3N signal intensity for the Li electrode cycled in PNF than in P(PEGMEA). Orbital energy diagram analysis suggests that Li_3N in P(PEGMEA) originates from the limited decomposition of $TFSI^-$ at the lithium surface. In contrast, Li_3N in PNF also derives from reduction reactions of PN at the lithium metal interface, thus yielding higher Li_3N content. As an inorganic SEI component with high ionic conductivity, Li_3N facilitates accelerated Li^+ migration and reduced interfacial

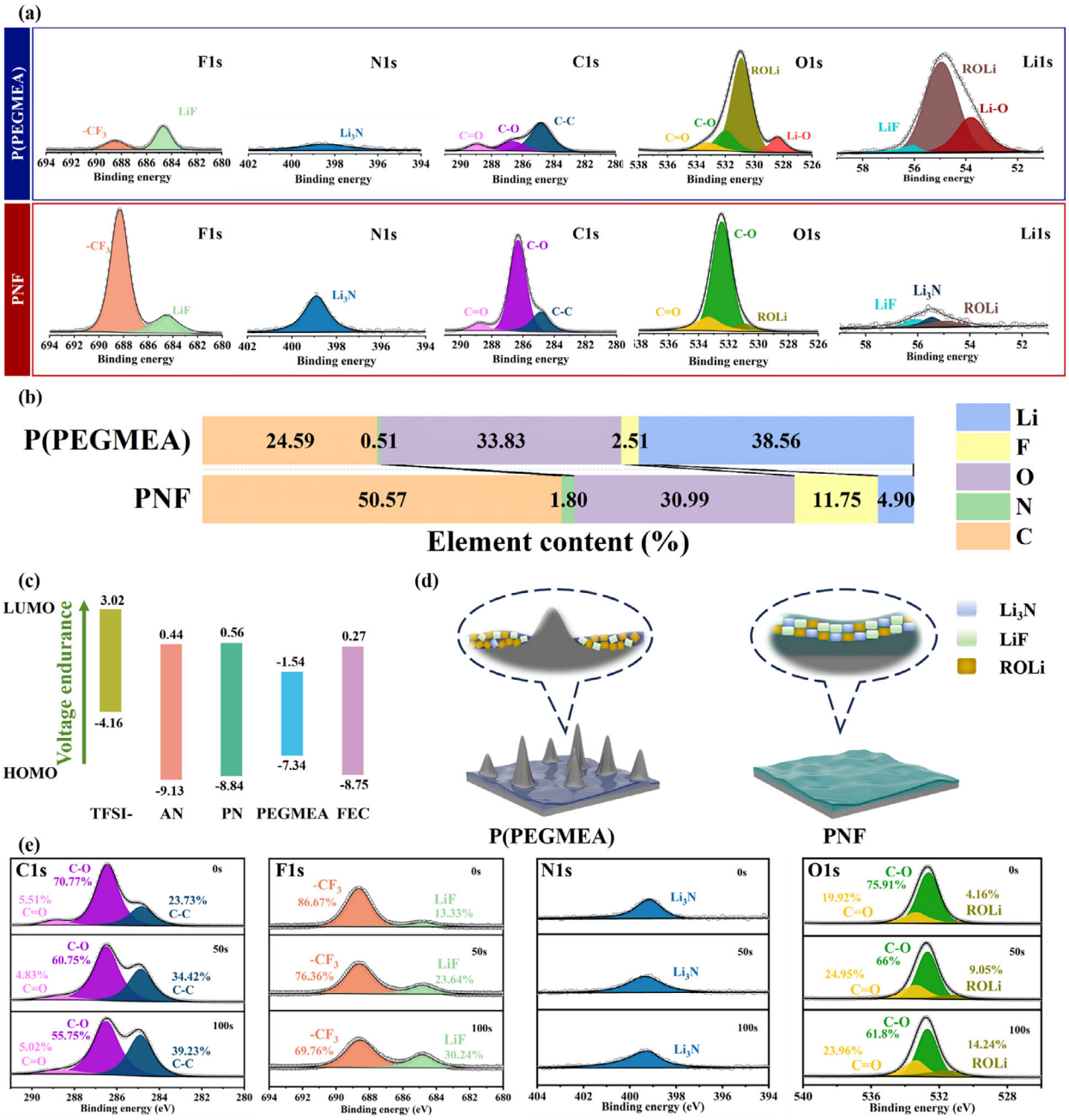

FIGURE 4 | (a) XPS spectra of Li electrodes extracted from Li|PNF|Li and Li|P(PEGMEA)|Li symmetric cells after 50 cycles. (b) Contents of various elements (atomic ratio), including C, N, O, F, and Li. (c) HOMO and LUMO levels of $TFSI^-$, AN, PN, PEGMEA, and FEC. (d) Schematic diagram of the SEI layer on the Li metal surface with PNF and P(PEGMEA). (e) Depth-profiling XPS spectra of the Li electrode from a cycled Li|PNF|Li cell.

resistance, thereby serving as a beneficial constituent for constructing robust SEI layers [38, 39]. Comparative analysis of C1s and O1s spectra reveals significantly attenuated C—O peak intensities in P(PEGMEA) relative to the PNF. Notably, P(PEGMEA) exhibits a prominent ROLi peak at 530.9 eV in O1s spectra. Orbital energy level analysis indicates that PEGMEA chains undergo side reactions with lithium metal during cycling, leading to polymer decomposition and ROLi generation. As an organic SEI component, ROLi forms a porous, flexible layer that accommodates minor lithium surface volume fluctuations; however, its low ionic conductivity and thermodynamic instability detrimentally impact cycling performance [40, 41]. In the P(PEGMEA) system, severe side reaction at the lithium surface generates substantial amounts of ROLi with concomitant decrease of C—O functional groups. Conversely, PNF exhibits fewer side reactions, generating only trace amounts of ROLi, these ROLi made the SEI more flexible to accommodate lithium volume changes without compromising cell performance. A schematic diagram depicting the structure of the SEI layer is presented in Figure 4d. In summary, within the PNF system, the Li_3N-rich component promotes rapid lithium-ion transport at the anode–electrolyte interface [42], while LiF suppresses electron transfer due to its electronically insulating nature, thereby inhibiting lithium dendrite growth [37]. The flexible ROLi component fills the gaps between inorganic phases such as LiF and Li_3N. This structure enables elastic deformation of the SEI, buffering the

stress induced by lithium metal volume changes during cycling. SEM images of the cycled lithium metal anode (Figure 3g,h) show a smooth and intact morphology with no dendritic features from uneven deposition. Furthermore, evidence from the Li1s spectra indicates that the organic–inorganic hybrid composite SEI layer of the PNF system, containing a balanced composition of LiF, Li_3N, and ROLi, ensures excellent performance during cycling. In contrast, the SEI layer formed with P(PEGMEA) is predominantly composed of low-ionic-conductivity LiF and ROLi, which raise the energy barrier for Li^+ migration, increase interfacial impedance, and hinder ion transport. These results are well aligned with the previous SEM and EIS data.

To probe the composition and structure of the SEI layer, XPS sputtering with Ar^+ was conducted (Figure 4e). The F1s and O1s spectra reveal that the signals for LiF and ROLi intensify with increasing sputtering time. Additionally, the N 1s spectrum indicates a uniform distribution of the Li_3N signal throughout the SEI layer. These results demonstrate the structural integrity of the SEI with a hybrid organic–inorganic composition, confirming that this balanced structure is not merely a surface phenomenon but it extends into the bulk of the layer.

2.4 | Cycling Performance of Full Cells and Pouch Cells

Li|PNF|$LiFePO_4$ cells were assembled to perform comprehensive testing. Figure 5a,b illustrate the rate capability along with the corresponding charge and discharge profiles, respectively. The specific capacity at 0.1, 0.2, 0.5, 1, and 2C rates (1C = 170 mA g^{-1}) were 155, 152, 143, 125, and 86 mAh g^{-1}, respectively. Upon restoring the C-rate to 0.1C, the discharge capacity returned to 155 mAh g^{-1}, demonstrating excellent capacity retention. As shown in Figure 5b, the charge/discharge voltage curves of the Li|PNF|$LiFePO_4$ cell remained stable across different rates. Additionally, the cell was tested at 0.1C °C and 0°C (Figure S16), demonstrating a specific capacity of 110 mAh g^{-1} while maintaining stable cycling performance. These indicate that PNF facilitates rapid Li^+ transport during cycling without significant side reactions. To further investigate the cycling performance of the full cell, the Li|PNF|$LiFePO_4$ and Li|P(PEGMEA)|$LiFePO_4$ cells were tested at 1C and 30°C (Figure 5c). Conducting five activation cycles at 0.1C, 0.2C, and 0.5C, followed by a charge/discharge test at 1C during the 16th cycle. In the case of the PNF system, the discharge capacity at the 16th cycle was 132 mAh g^{-1}, markedly exceeding the 84 mAh g^{-1} observed for the P(PEGMEA) system. The Li|PNF|$LiFePO_4$ cell demonstrated cycling capability for up to 2000 cycles with a capacity retention of 78.9%. After 1000 cycles, the cell's capacity retention was 88.2%. In contrast, P(PEGMEA) exhibited significant capacity degradation from the beginning, indicating that PNF possesses superior Li^+ transport capability, hence guaranteeing steady battery performance at elevated rates. Subsequently, the cycling performance of the Li|PNF|$LiFePO_4$ cell at 0.5C and 30°C was evaluated, after formation with five cycles at both 0.1C and 0.2C. Remarkably, after 1000 cycles, the cell capacity retention was 92.6%. Furthermore, the charge/discharge voltage curves of the Li|PNF|$LiFePO_4$ cell at varying cycle counts under 1C and 0.5C were analyzed (Figure S17a,b). With the exception of slight capacity degradation, the charge/discharge curves exhibited stability, indicating remarkable cycling endurance. Figure 5e compares the cycling performance of PNF with that of the reported PEGMEA-based solid electrolytes [17–19, 43–47]. PNF outperformed other PEGMEA-based solid electrolytes in terms of cycle life and capacity retention, primarily due to the enhanced transport of lithium ions and compatibility with lithium metal, both of which promote uniform lithium deposition. After cycling at 0.5C for 1000 cycles, conducting SEM characterization of the lithium metal surface of the battery (Figure 6a,b). The results indicated that even after prolonged cycling, the lithium surface remained smooth and uniform, with a consistent composite interfacial layer observed in the cross-sectional SEM images.

Motivated by the prior outcomes, Li|PNF|NCM622 cells were assembled and evaluated under two conditions: 0.5C at 45°C (Figure S18a) and 0.1C at 30°C (Figure S18b). Following three activation cycles at 0.1C and 0.2C, the initial capacity at 0.5C (45°C) was 130.8 mAh g^{-1}, and it retained 86.4% of its capacity after 150 cycles. At 0.1C °C and 30°C, the initial specific capacity was 129.3 mAh g^{-1}, reaching a maximum of 137 mAh g^{-1} after 16 cycles, with a capacity retention of 84% after 160 cycles, the corresponding charge/discharge curves are shown in Figure S18c,d. In addition, XPS investigation was performed on the cycled NCM622 electrode surface (Figure S19). The strong signal peaks corresponding to -CN and TM-CN in the N1s and C1s spectra indicate that the PN plasticizer, with its higher HOMO energy level, preferentially reacts at the cathode side and participates in the formation of the CEI. A small amount of LiF detected in the F1s spectrum mainly originates from the decomposition of fluorine-containing components (LiTFSI and FEC) in the electrolyte at the interface. The aforementioned interfacial layer, particularly the formation of TM-CN complexes, can effectively anchor dissolved transition metal ions, thereby potentially inhibiting their continued dissolution. This contributes to enhancing the structural and cycling stability of the cathode [48, 49]. These findings suggest the feasibility of PNF in conjunction with high-voltage cathodes. To further validate the practical applicability of PNF, pouch cells were assembled and tested. Figure 6c illustrates the cycling performance of the Li|PNF|$LiFePO_4$ pouch cell, which cycled stably for 100 cycles at 0.1C and room temperature. The charge/discharge curves shown in Figure 6d exhibited high stability, with a specific capacity reaching 163 mAh g^{-1} and negligible capacity decay, demonstrating excellent cycling stability. To further evaluate the flexibility and safety of the pouch cell, various tests under harsh conditions were performed, including bending, cutting, and puncturing, as depicted in Figure 6f–i. Remarkably, even under these extreme testing conditions, the PNF-based pouch cell consistently provided stable current to power an LED light board. Moreover, no safety concerns, including smoke or fire, were detected during these harsh tests, indicating the superior safety and practicality of PNF.

3 | Conclusion

In summary, a PEGMEA-based PSE was developed through in situ polymerization. The incorporated PN, which utilizes the strong electron-withdrawing nature of its —C≡N group, enhances Li^+ dissociation from LiTFSI and provides additional Li^+ hopping sites. This establishes novel Li^+ transport pathways within PNF,

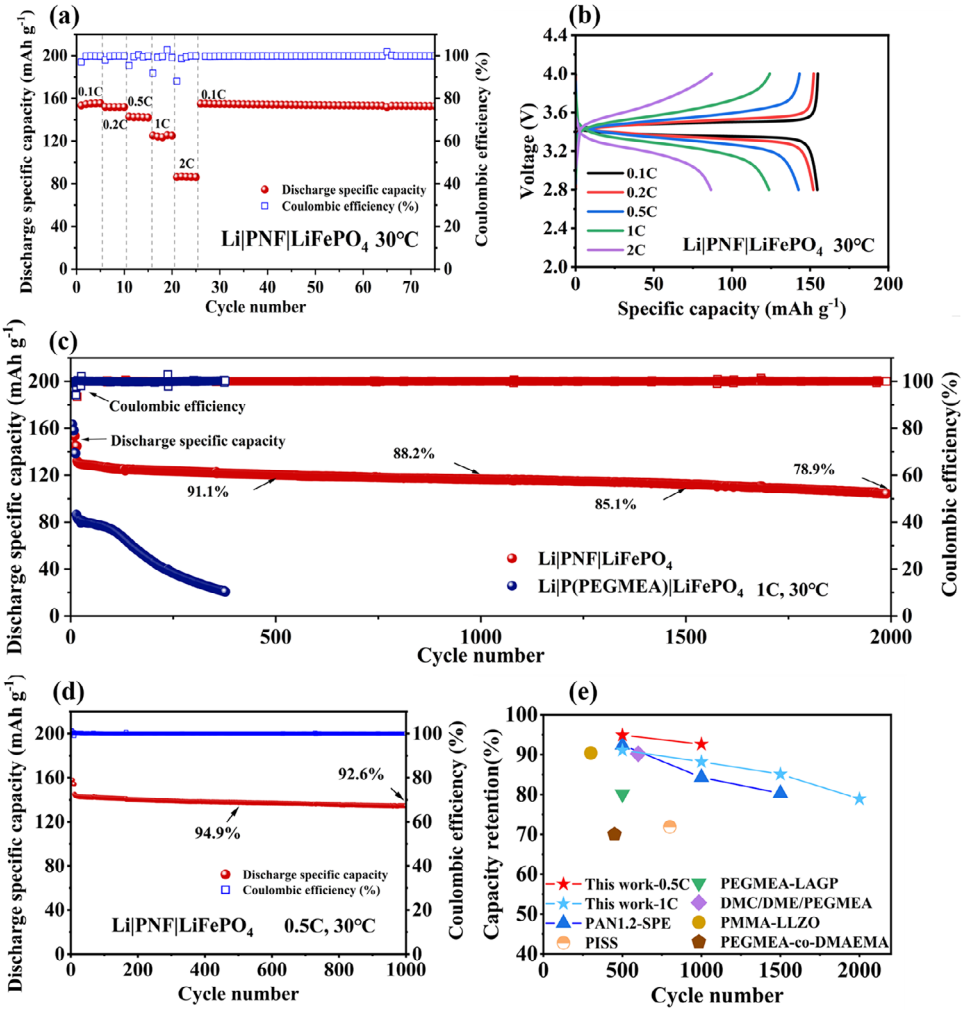

FIGURE 5 | (a) Rate performance of Li|PNF|LiFePO$_4$ cell and (b) corresponding charged/discharge curves at different rates. Long-term cycling performance of the Li|PNF|LiFePO$_4$ and Li|P(PEGMEA)|LiFePO$_4$ cell (c) at 1C and (d) at 0.5C. (e) Comparison of the cycling performance with other PEGMEA-based electrolytes.

achieving an ionic conductivity of 3.47×10^{-4} S cm^{-1} at 30°C. Simultaneously, the fully methylated PN significantly improves reduction stability against lithium metal in the PNF system, forming a hybrid organic–inorganic SEI layer with a balanced rigidity and flexibility. Consequently, Li|PNF|Li symmetric cells demonstrate stable plating and stripping for over 1000 h at current densities of 0.3 and 0.5 mA cm^{-2}. Furthermore, Li|PNF|LiFePO$_4$ cells demonstrate exceptional long-term cycling stability, retaining 78.9% of capacity after 2000 cycles at 1C rate and 30°C. The assembled Li|PNF|LiFePO$_4$ pouch cell also shows outstanding cyclability and safety. The PNF PSE design establishes a strategic framework for developing long-lasting and safe SLMBs.

4 | Experimental Section

4.1 | Materials

Pivalonitrile (PN), fluoroethylene carbonate (FEC), poly(ethylene glycol) methyl ether acrylate (PEGMEA), lithium bis(trifluoromethanesulfonyl)imide (LiTFSI), acetonitrile (AN), and 2,2'-azobis(2-methylpropionitrile) (AIBN) were obtained from Shanghai Aladdin Biochemical Technology Co., Ltd. All materials were stored and handled in an argon-filled glove box (<0.01 ppm O_2 and <0.01 ppm H_2O) with continuous gas circulation.

4.2 | Electrolyte Preparation

First, 700 μL PEGMEA (0.76 g), 300 μL PN (0.22 g), and LiTFSI (0.287 g) were mixed to form a 1 M solution of LiTFSI in the PEGMEA: PN (7:3 vol/vol) mixture. Then, FEC (10 wt.%) was added to the mixture and stirred until homogeneity was achieved. Finally, AIBN (0.5 wt.%) was introduced as a free-radical polymerization initiator to yield PNF-LE (electrolyte precursor solution). This precursor was injected into the GFA separator, and the system was assembled into a 2032-coin cell. Finally, the assembled cell was heated at 65°C for 12 h to form the PNF solid polymer electrolyte. PNFx (where x = 1,2,3,4,5) represents mixtures of PEGMEA and PN with volumetric ratios of 9:1, 8:2, 7:3, 6:4, and 5:5, respectively. PAF was synthesized by replacing PN with AN while maintaining identical preparation procedures to PNF. P(PEGMEA) was synthesized by uniformly

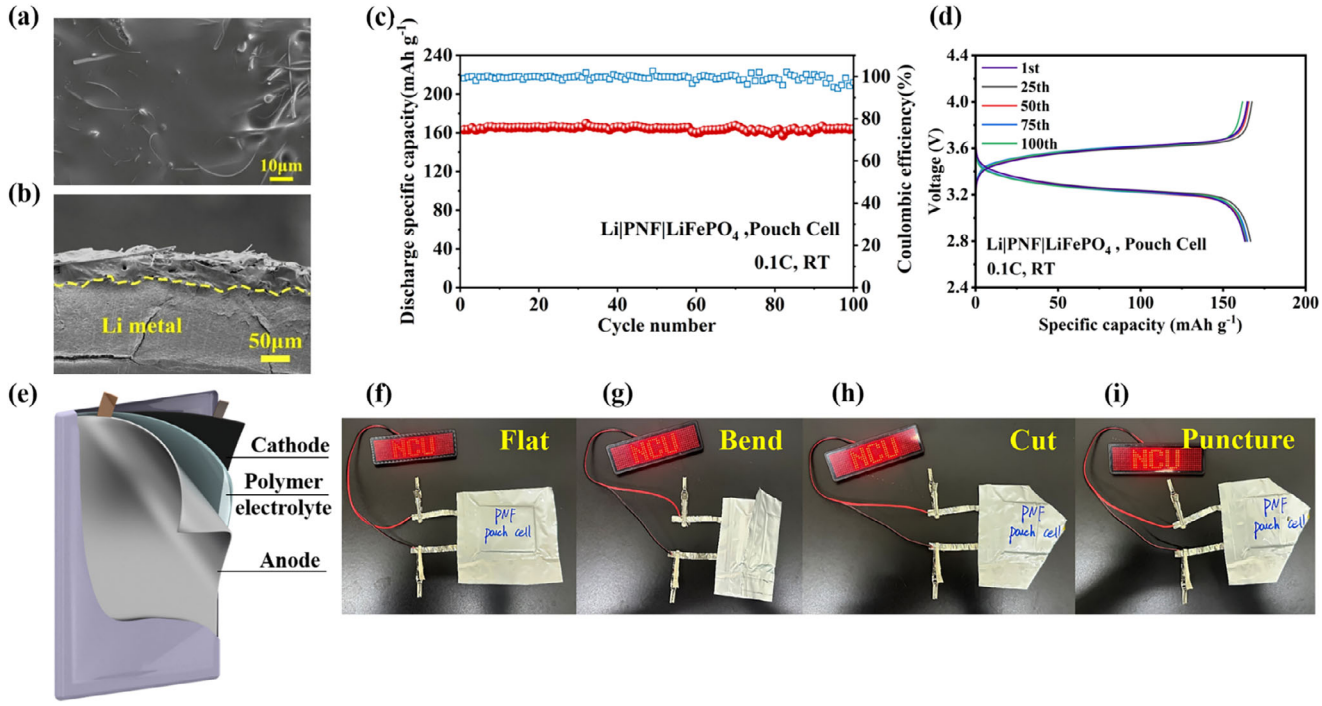

FIGURE 6 | (a) Surface and (b) cross-sectional SEM images of Li metal anode collected from Li|PNF|$LiFePO_4$ cell after 1000 cycles. (c) Cycling performance of Li|PNF|$LiFePO_4$ pouch cell at 0.1C and (d) selected charge/discharge curves. (e) Schematic diagram of a pouch cell with PNF electrolyte. (f–i) Safety test, involving bending, cutting, and puncturing (in sequence) of a cell lighting a LED panel.

mixing 1 M LiTFSI with PEGMEA, adding 0.5wt.% AIBN, and polymerizing at 65°C for 12 h.

4.3 | Cathode Preparation

$LiFePO_4$ cathodes were fabricated by mixing $LiFePO_4$, Super P, and polyvinylidene fluoride (PVDF) at a 7:2:1 mass ratio in N-methyl-2-pyrrolidone (NMP) solvent to form a cathode slurry. The slurry was coated onto aluminum foil, vacuum-dried at 80°C for 12 h, and punched into 12 mm diameter electrodes with an active material mass loading of 1.5–2 mg cm^{-2}. All electrodes were stored in an argon-filled glove box (<0.01 ppm O_2 and <0.01 ppm H_2O).

NCM622 cathodes were prepared by mixing $LiNi_{0.6}Co_{0.2}Mn_{0.2}O_2$ (NCM622) powder, Super P, and polyvinylidene fluoride (PVDF) at an 8:1:1 mass ratio in N-methyl-2-pyrrolidone (NMP) solvent to form a cathode slurry. The slurry was coated onto aluminum foil, vacuum-dried at 80°C for 12 h, and punched into 12 mm diameter electrodes with an active material mass loading of 1–1.5 mg cm^{-2}. All electrodes were stored in an argon-filled glove box (<0.01 ppm O_2 and <0.01 ppm H_2O).

4.4 | Material Characterizations

Fourier-transform infrared spectroscopy (FTIR) was performed using a Thermo Fisher Scientific Nicolet iS20 spectrometer. X-ray photoelectron spectroscopy (XPS) measurements were conducted on a Thermo Fisher Scientific K-Alpha XPS spectrometer. Scanning electron microscopy (SEM) images of cycled lithium metal surfaces and electrolytes were acquired with a ZEISS Gemini SEM 300 high-resolution field-emission scanning electron microscope. Thermogravimetric analysis (TGA) was carried out on a METTLER TOLEDO instrument under argon atmosphere at a heating rate of 10°C min^{-1}.

4.5 | Electrochemical Characterizations

The electrochemical performance of the prepared polymer electrolytes were measured by a Ivium Technologies nSTAT electrochemical workstation. Electrochemical impedance spectroscopy (EIS) was recorded from 30°C to 80°C in the frequency range from 0.1 Hz to 100k Hz and an AC amplitude of 10 mV.

$$\sigma = d/R \cdot S$$

where d presents the thickness of the membrane, R represents the resistance, and S is the contact area between Stainless steel (SS) and the electrolyte membrane.

The activation energy E_a for the Li^+ conduction was calculated according to the Arrhenius equation:

$$\sigma = A \cdot \exp(-E_a/k_b T)$$

where A is the pre-exponential factor, k_b presents the Boltzmann constant, T is the absolute temperature, E_a is the activation energy.

The lithium ions transference number t_{Li^+} was examined via direct-current (DC) polarization combined with AC impedance in a Li|Li symmetric cell. The t_{Li^+} values were calculated according

to the Bruce–Vincent–Evans equation:

$$t_{Li^+} = I_s\left(\Delta V - I_0 R_0\right)/I_0\left(\Delta V - I_s R_s\right)$$

where ΔV is the applied DC potential (10 mV), I is the measured current, and R is the charge-transfer resistance. The "0" and "S" subscripts represent the initial and steady state, respectively.

Linear sweep voltammetry (LSV) measurements were conducted on the SS|Li unsymmetrical cell with a scan rate of 0.1 mV/s. The galvanostatic charge/discharge tests were recorded on a NEWARE testing system.

Authorship contribution statement

L.H. contributed to data curation, formal analysis, investigation, methodology, validation, and writing the original draft. L.L. and Y.W. contributed to methodology, formal analysis, and validation. X.A. contributed to methodology and formal analysis. N.Z. and Y.Z. contributed to formal analysis and validation. C.P. and Y.L. contributed to formal analysis. S.F. contributed to resources, supervision, project administration, funding acquisition, conceptualization, and writing – review and editing. Stefano Passerini contributed to conceptualization, supervision, and writing – review and editing.

Acknowledgements

Project funded by the National Natural Science Foundation of China (52161039, 52472297). Jiangxi Provincial Natural Science Foundation (20252BAC210010), Talent Project of Double Thousands Plan in Jiangxi Province (jxsq2020101056). SP acknowledge the basic funding of Helmholtz Association.

Open access funding enabled and organized by Projekt DEAL.

Conflicts of Interest

The authors declare no conflicts of interest.

Data Availability Statement

The data that support the findings of this study are available from the corresponding author upon reasonable request.

References

1. X. Li, F. Luo, N. Zhou, et al., "Weakly Solvating Electrolytes for Lithium and Post-Lithium Rechargeable Batteries: Progress and Outlook," *Advanced Energy Materials* 15 (2025): 2501272, https://doi.org/10.1002/aenm.202501272.

2. J.-H. Kim, N.-Y. Kim, Z. Ju, et al., "Upscaling High-Areal-Capacity Battery Electrodes," *Nature Energy* 10 (2025): 295–307, https://doi.org/10.1038/s41560-025-01720-0.

3. X. Zhang, S. Cheng, C. Fu, et al., "Advancements and Challenges in Organic–Inorganic Composite Solid Electrolytes For All-Solid-State Lithium Batteries," *Nano-Micro Letters* 17 (2024): 2.

4. L. Jia, J. Zhu, X. Zhang, B. Guo, Y. Du, and X. Zhuang, "Li–Solid Electrolyte Interfaces/Interphases in All-Solid-State Li Batteries," *Electrochemical Energy Reviews* 7 (2024): 12, https://doi.org/10.1007/s41918-024-00212-1.

5. X. Lu, Y. Wang, X. Xu, B. Yan, T. Wu, and L. Lu, "Polymer-Based Solid-State Electrolytes for High-Energy-Density Lithium-Ion Batteries—Review," *Advanced Energy Materials* 13 (2023): 2301746, https://doi.org/10.1002/aenm.202301746.

6. C.-Z. Zhao, B.-C. Zhao, C. Yan, et al., "Liquid Phase Therapy to Solid Electrolyte–Electrode Interface in Solid-State Li Metal Batteries: A review," *Energy Storage Materials* 24 (2020): 75–84, https://doi.org/10.1016/j.ensm.2019.07.026.

7. S. Kim, M. J. Lee, S. H. Kwon, et al., "Designing Isocyanate-Containing Elastomeric Electrolytes for Antioxidative Interphases in 4.7 V Solid-State Lithium Metal Batteries," *Advanced Energy Materials* 14 (2024): 2403846, https://doi.org/10.1002/aenm.202403846.

8. L.-Z. Fan, H. He, and C.-W. Nan, "Tailoring Inorganic–Polymer Composites for the Mass Production of Solid-State Batteries," *Nature Reviews Materials* 6 (2021): 1003–1019, https://doi.org/10.1038/s41578-021-00320-0.

9. S. Zou, Y. Yang, J. Wang, et al., "In Situ Polymerization of Solid-State Polymer Electrolytes for Lithium Metal Batteries: A Review," *Energy & Environmental Science* 17 (2024): 4426–4460, https://doi.org/10.1039/D4EE00822G.

10. Y. Tong, B. Chen, C. Liu, et al., "Achieving an Ultrastable Halide-Based All-Solid-State Lithium Battery via High-Valent Doping-Induced s-p-d Hybridization," *Advanced Functional Materials* 35 (2025): 2502201, https://doi.org/10.1002/adfm.202502201.

11. Z. Song, F. Chen, M. Martinez-Ibañez, et al., "A reflection on Polymer Electrolytes for Solid-State Lithium Metal Batteries," *Nature Communications* 14 (2023): 4884, https://doi.org/10.1038/s41467-023-40609-y.

12. X. Zeng, X. Liu, H. Zhu, et al., "Advanced Crosslinked Solid Polymer Electrolytes: Molecular Architecture, Strategies, and Future Perspectives," *Advanced Energy Materials* 14 (2024): 2402671, https://doi.org/10.1002/aenm.202402671.

13. X. Su, X.-P. Xu, Z.-Q. Ji, J. Wu, F. Ma, and L.-Z. Fan, "Polyethylene Oxide-Based Composite Solid Electrolytes for Lithium Batteries: Current Progress, Low-Temperature and High-Voltage Limitations, and Prospects," *Electrochemical Energy Reviews* 7 (2024): 2, https://doi.org/10.1007/s41918-023-00204-7.

14. S. Zhang, B. Xie, X. Zhuang, et al., "Great Challenges and New Paradigm of The In Situ Polymerization Technology Inside Lithium Batteries," *Advanced Functional Materials* 34 (2024): 2314063, https://doi.org/10.1002/adfm.202314063.

15. J. Park, H. Seong, C. Yuk, et al., "Design of Fluorinated Elastomeric Electrolyte for Solid-State Lithium Metal Batteries Operating at Low Temperature and High Voltage," *Advanced Materials* 36 (2024): 2403191, https://doi.org/10.1002/adma.202403191.

16. G. Xiao, H. Xu, C. Bai, M. Liu, and Y.-B. He, "Progress and Perspectives of In Situ Polymerization Method for Lithium-Based Batteries," *Interdisciplinary Materials* 2 (2023): 609–634, https://doi.org/10.1002/idm2.12109.

17. Y. Yan, J. Ju, S. Dong, et al., "In Situ Polymerization Permeated Three-Dimensional Li + -Percolated Porous Oxide Ceramic Framework Boosting All Solid-State Lithium Metal Battery," *Advanced Science* 8 (2021): 2003887, https://doi.org/10.1002/advs.202003887.

18. Y. Wang, J. Ju, S. Dong, et al., "Facile Design of Sulfide-Based all Solid-State Lithium Metal Battery: In Situ Polymerization Within Self-Supported Porous Argyrodite Skeleton," *Advanced Functional Materials* 31 (2021): 2101523, https://doi.org/10.1002/adfm.202101523.

19. D. Zhang, Y. Liu, Z. Sun, et al., "Eutectic-Based Polymer Electrolyte With the Enhanced Lithium Salt Dissociation for High-Performance Lithium Metal Batteries," *Angewandte Chemie International Edition* 62 (2023): 202310006, https://doi.org/10.1002/anie.202310006.

20. X. Ye, H. Fu, Y. Zhang, et al., "Modulating the Li-Ion Transport Pathway of Succinonitrile-Based Plastic Crystalline Electrolytes for Solid-State Lithium Metal Batteries," *Advanced Functional Materials* 35 (2025): 2413205, https://doi.org/10.1002/adfm.202413205.

21. R. Yan, K. Zhang, B. Li, et al., "Nitrile-Based Solid Polymer Electrolytes for Novel Energy Storage Systems: A Perspective from ion Transport Mechanism to Applications in Solid-State Batteries," *Energy Storage Materials* 79 (2025): 104317, https://doi.org/10.1016/j.ensm.2025.104317.

22. J. Han, M. J. Lee, K. Lee, et al., "Role of Bicontinuous Structure in Elastomeric Electrolytes for High-Energy Solid-State Lithium-Metal Batteries," *Advanced Materials* 35 (2023): 2205194, https://doi.org/10.1002/adma.202205194.

23. C. Su, Y. Qu, N. Hu, et al., "Rapid Na + Transport Pathway and Stable Interface Design Enabling Ultralong Life Solid-State Sodium Metal Batteries," *Angewandte Chemie International Edition* 64 (2025): 202418959, https://doi.org/10.1002/anie.202418959.

24. L. Zhao, A. Xu, Y. Cheng, H. Xu, L. Xu, and L. Mai, "A Highly Stable and Non-Flammable Deep Eutectic Electrolyte for High-Performance Lithium Metal Batteries," *Angewandte Chemie International Edition* 63 (2024): 202411224.

25. W. Li, S. Han, C. Xiao, et al., "High-Voltage Single-Ion Covalent Organic Framework Electrolytes Enabled by Nitrile Migration Ladders for Lithium Metal Batteries," *Angewandte Chemie International Edition* 63 (2024): 202410392.

26. J. Ma, Z. Wang, J. Wu, Z. Gu, X. Xin, and X. Yao, "In Situ Solidified Gel Polymer Electrolytes for Stable Solid−State Lithium Batteries at High Temperatures," *Batteries* 2023, 9, 28.

27. Z. Wang, L. Shen, S. Deng, P. Cui, and X. Yao, "10 μm-Thick High-Strength Solid Polymer Electrolytes With Excellent Interface Compatibility for Flexible All-Solid-State Lithium-Metal Batteries," *Advanced Materials* 33 (2021): 2100353, https://doi.org/10.1002/adma.202100353.

28. S. Li, S. Fang, Z. Li, W. Chen, H. Dou, and X. Zhang, "A High-Voltage Lithium-Metal Batteries Electrolyte Based on Fully-Methylated Pivalonitrile," *Batteries & Supercaps* 5 (2022): 202100416.

29. Z. Li, J. Fu, X. Zhou, et al., "Ionic Conduction in Polymer-Based Solid Electrolytes," *Advanced Science* 10 (2023): 2201718, https://doi.org/10.1002/advs.202201718.

30. Y. Gong, C. Wang, M. Xin, et al., "Ultra-thin and high-voltage-stable Bi-phasic solid polymer electrolytes for high-energy-density Li metal batteries," *Nano Energy* 119 (2024): 109054, https://doi.org/10.1016/j.nanoen.2023.109054.

31. L. Edman, "Ion Association and Ion Solvation Effects at the Crystalline−Amorphous Phase Transition in PEO−LiTFSI," *The Journal of Physical Chemistry B* 104 (2000): 7254–7258, https://doi.org/10.1021/jp000082d.

32. X. Lin, J. Yu, M. B. Effat, et al., "Ultrathin and Non-Flammable Dual-Salt Polymer Electrolyte for High-Energy-Density Lithium-Metal Battery," *Advanced Functional Materials* 31 (2021): 2010261, https://doi.org/10.1002/adfm.202010261.

33. Z. Hu, F. Xian, Z. Guo, et al., "Nonflammable Nitrile Deep Eutectic Electrolyte Enables High-Voltage Lithium Metal Batteries," *Chemistry of Materials* 32 (2020): 3405–3413, https://doi.org/10.1021/acs.chemmater.9b05003.

34. C. Lin, T. Yang, H. Zhang, et al., "Ternary Stabilization Strategies for Succinonitrile-Based In Situ Polymerized Electrolyte Enabling High-Performance Solid Lithium Metal Batteries," *Chemical Engineering Journal* 495 (2024): 153541, https://doi.org/10.1016/j.cej.2024.153541.

35. X. Zhao, C. Wang, H. Liu, Y. Liang, and L.-Z. Fan, "A Review of Polymer-Based Solid-State Electrolytes for Lithium-Metal Batteries: Structure, Kinetic, Interface Stability, and Application," *Batteries & Supercaps* 6 (2023): 202200502.

36. T. Wang, X. Liu, S. Huang, et al., "Development of polymer-based artificial solid electrolyte interphase for safer Li-metal batteries: Challenges, strategies and prospects," *Nano Energy* 129 (2024): 109970, https://doi.org/10.1016/j.nanoen.2024.109970.

37. Y. Zheng, N. Yang, S. Duan, et al., "Dual-Enhanced Charge Transfer through Prelithiation Strategy in Polymer Electrolyte Enables Robust LiF-Rich SEI for Ultralong-Life All-Solid-State Batteries," *Advanced Functional Materials* 11011.

38. M. S. Kim, Z. Zhang, J. Wang, et al., "Revealing the Multifunctions of Li 3 N in the Suspension Electrolyte for Lithium Metal Batteries," *ACS Nano* 17 (2023): 3168–3180, https://doi.org/10.1021/acsnano.2c12470.

39. Y. Li, A. Hu, X. Gan, et al., "Synergy of in situ heterogeneous interphases tailored lithium deposition," *Nano Research* 16 (2023): 8304–8312, https://doi.org/10.1007/s12274-022-5004-0.

40. D. Kang, S. Sardar, R. Zhang, et al., "In situ organic SEI layer for dendrite-free lithium metal anode," *Energy Storage Materials* 27 (2020): 69–77, https://doi.org/10.1016/j.ensm.2020.01.020.

41. D. Kang, N. Hart, J. Koh, et al., "Rearrange SEI with Artificial Organic Layer For Stable Lithium Metal Anode," *Energy Storage Materials* 24 (2020): 618–625, https://doi.org/10.1016/j.ensm.2019.06.014.

42. X. Wang, Q. Chen, S. Gui, et al., "In Situ Construction of Inorganic-Rich Solid Electrolyte Interphase via Selective Anode-Electrolyte Interactions Enabling Stable Lithium Metal Batteries," *Advanced Functional Materials* 20120.

43. B. Azhar, Q.-T. Pham, Y.-S. Wu, et al., "Copolymers Comprising Poly(Ethylene Glycol) Acrylate Soft Unit and Sulfobetaine Methacrylate Zwitterionic Unit and its Application in Solid-State Lithium Metal Battery at Ambient Temperature," *Electrochimica Acta* 480 (2024): 143920, https://doi.org/10.1016/j.electacta.2024.143920.

44. Y. Zhai, W. Hou, M. Tao, et al., "Enabling High-Voltage "Superconcentrated Ionogel-in-Ceramic" Hybrid Electrolyte With Ultrahigh Ionic Conductivity and Single Li + -Ion Transference Number," *Advanced Materials* 34 (2022): 2205560, https://doi.org/10.1002/adma.202205560.

45. K. Zhang, F. Wu, X. Wang, et al., "8.5 μ m-Thick Flexible-Rigid Hybrid Solid–Electrolyte/Lithium Integration for Air-Stable and Interface-Compatible All-Solid-State Lithium Metal Batteries," *Advanced Energy Materials* 12 (2022): 2200368, https://doi.org/10.1002/aenm.202200368.

46. J. Wang, C. Tao, J. Cao, X. Jiao, L. Wang, and T. Liu, "A Quasi-Solid Electrolyte by In Situ Polymerization of Selective Solvent for Lithium-Metal Batteries," *ChemElectroChem* 9 (2022): 202200957.

47. J. Yang, R. Li, P. Zhang, et al., "Crosslinked polymer-in-salt solid electrolyte With multiple ion transport paths for solid-state lithium metal batteries," *Energy Storage Materials* 64 (2024): 103088, https://doi.org/10.1016/j.ensm.2023.103088.

48. X. Li, Y. Bai, J. Jing, et al., "Cyano-Functionalized Hybrid Electrode-Electrolyte Interphases Enabled by Cyano-Substituted Tetrafluorobenzene Derivatives Additives for High-Voltage Lithium Metal Batteries," *Advanced Functional Materials* 35 (2025): 2421329, https://doi.org/10.1002/adfm.202421329.

49. D. Zhou, Z. Yang, S. Wang, et al., "Enhancing cycling stability of Li-rich Mn-based cathode materials via cyano functional additives," *Materials Chemistry Frontiers* 9 (2025): 965–975, https://doi.org/10.1039/D4QM01070A.

Supporting Information

Additional supporting information can be found online in the Supporting Information section.

Supporting Information File 1: adfm73673-sup-0001-SuppMat.docx